Soft Matter

RSC Publishing

PAPER

View Article Online
View Journal | View Issue

Viscoelastic effects on electromechanical instabilities in dielectric elastomers

Cite this: *Soft Matter*, 2013, **9**, 1031

Harold S. Park*[a] and Thao D. Nguyen[b]

We present a computational study of the effects of viscoelasticity on the electromechanical behavior of dielectric elastomers. A dynamic, finite deformation finite element formulation for dielectric elastomers is developed that incorporates the effects of viscoelasticity using the nonlinear viscoelasticity theory previously proposed by Reese and Govindjee. The finite element model features a three-field Q1P0 formulation to alleviate volumetric locking effects caused by material incompressibility. We apply the formulation to first perform a fundamental examination of the effects of the viscoelastic deviatoric and volumetric response on dielectric elastomers undergoing homogeneous deformation. Specifically, we evaluate the effects of the shear and bulk relaxation times on the electromechanical instability, and demonstrate that while the bulk relaxation time has a negligible impact, the shear relaxation time substantially increases the critical electric field needed to induce electromechanical instability. We also demonstrate a significant increase in the critical voltage needed to induce electromechanical instability in the presence of a distribution of relaxation times, compared to a single relaxation time, where the former is more representative of viscoelastic behavior of polymers. We then study the effects of viscoelasticity on crack-like electromechanical instabilities that have recently been observed in constrained dielectric films with a small hole containing a conductive liquid. Viscoelasticity is shown again to not only significantly increase the critical electric field to induce the electromechanical instability, but also to substantially reduce the crack propagation speeds in the elastomer.

Received 15th October 2012
Accepted 22nd November 2012

DOI: 10.1039/c2sm27375f

www.rsc.org/softmatter

1 Introduction

Dielectric elastomers (DEs) have attracted significant attention in recent years as a soft and flexible actuation material.[2–4] The salient characteristic of DEs is that if sandwiched between two compliant electrodes that apply voltage across the thickness, the DE can exhibit both significant thinning and in-plane expansion, where the in-plane expansion can often exceed several hundred percent.[5] The ability to undergo such large deformations has led to DEs being studied for both actuation-based applications, including artificial muscles and flexible electronics, as well as for generation-based applications and energy harvesting.[2,3,6]

In-depth investigation of the mechanical behavior of DEs began with the seminal experimental work of Pelrine *et al.*[7,8] Since then, there have been many experimental,[9–23] theoretical,[15,16,24–31] and more recently, a small number of computational[31–36] studies aimed that identifying the mechanisms that have the greatest impact on the nonlinear dynamical behavior and failure of mechanisms of DEs.

From these extensive studies, it is now well-known that the electromechanical behavior and properties of DEs is strongly rate-dependent.[4,14,19,37] However, a quantitative characterization of viscoelastic effects on the nonlinear dynamics and failure mechanisms of DEs under external loading remains an open area for a number of reasons. First, while recent theoretical work has made progress in this direction,[38–40] the incorporation of complex viscoelastic constitutive relationships within an analytical model has led to difficulties in evaluating viscous effects on the failure mechanisms of DEs undergoing generalized electromechanical deformations. The viscoelastic behavior of polymers is characterized by broad distributions of relaxation times, though their behavior is often modeled by a single relaxation process. Consequently, elastomers can exhibit time-dependent properties over a broad range of time scales.[41] Viscoelastic behavior appears in both the shear and bulk response, but the effect is significantly larger in shear. The storage modulus for shear can change by a factor of 1000 through the transition between glassy and rubbery behavior, while the storage modulus for the volumetric response changes only by a factor of 2.[42] The tan delta, defined as the ratio of the loss to storage modulus, characterizes the viscous dissipation exhibited by a viscoelastic material at a given temperature and frequency. While the peak of the tan delta for the bulk and shear

[a]*Department of Mechanical Engineering, Boston University, Boston, MA 02215, USA. E-mail: parkhs@bu.edu; Fax: +1 617 353 5866; Tel: +1 617 353 4208*

[b]*Department of Mechanical Engineering, The Johns Hopkins University, Baltimore, MD 21218, USA. Fax: +1 410 516 7254; Tel: +1 410 516 4538*

response occurs at the same frequency, the tan delta for shear has a broader frequency range.

Second, while there have been a small number of computational models that have accounted for viscoelasticity,[43] these studies have been limited to linearized theories, which is incongruous with the large deformations that DEs undergo before the development of instabilities and subsequent failure. Linear and finite linear theories of viscoelasticity[44,45] inherently assume small perturbations from thermodynamic equilibrium, and cannot be applied in situations of large viscous deformations, such as creep. Nonlinear theories that incorporate the effects of large viscous deformation lead to faster creep and relaxation and smaller stresses compared to linear theories.[46,47]

Third, few existing computational models except for the recent, dynamic finite element model of Part *et al.*[32] have demonstrated the capability of capturing the dynamics and evolution of inhomogeneous deformation, *i.e.* wrinkles, electromechanical snap-through and creasing. These ongoing experimental and theoretical issues suggest that the fundamental mechanisms underlying the nonlinear dynamical behavior and properties that lead to instability and failure of DEs at large deformations, as illustrated by the establishment of complex wrinkling patterns in the work of Plante and Dubowsky,[14] or the more recent creasing instabilities observed by Wang *et al.*[21] and the crack-like failure mechanism seen by Wang *et al.*[23] are still not completely understood, particularly when viscous material effects are accounted for.

Therefore, we present a nonlinear, finite deformation finite element (FEM) model based on the previous work of Park *et al.*,[32] while incorporating viscoelastic effects using the fully finite deformation viscoelastic theory of Reese and Govindjee.[1] The resulting viscoelastic DEFEM model also significantly alleviates numerical volumetric locking effects caused by the incompressible nature of the DEs, by incorporating the three-field Q1P0 variational formulation of Simo *et al.*[48] We apply the model to perform fundamental studies of viscoelastic effects on the electromechanical behavior under homogeneous and inhomogeneous deformations. Lastly, we examine the effects of material viscoelasticity on crack-like electromechanical instabilities in constrained DEs.[23]

2 Background: nonlinear electromechanical field theory

Because the FEM methodology[32] and governing electromechanical field theory[24] we build upon in the present work have both previously been discussed in detail, we present only a brief overview here while referring the interested reader to the above references for a more complete development.

The numerical results we present in this work are based upon a FEM discretization of the electromechanical field theory recently proposed by Suo *et al.*,[24] and recently reviewed by Suo.[25] In this field theory at mechanical equilibrium, the nominal stress S_{iJ} satisfies the following weak form of the momentum balance equation:

$$\int_V S_{iJ}\frac{\partial \xi_i}{\partial X_J}\mathrm{d}V = \int_V \left(B_i - \rho\frac{\partial^2 x_i}{\partial t^2}\right)\xi_i \mathrm{d}V + \int_A T_i \xi_i \mathrm{d}A, \qquad (1)$$

where ξ_i is an arbitrary vector test function, B_i is the body force per unit reference volume V, ρ is the mass density of the material and T_i is the force per unit area that is applied on the surface A in the reference configuration.

For the electrostatic problem, the nominal electric displacement $\tilde{D}_I$ satisfies the following weak form of the governing equation:

$$-\int_V \tilde{D}_I \frac{\partial \eta}{\partial X_I}\mathrm{d}V = \int_V q\eta \mathrm{d}V + \int_A \omega\eta \mathrm{d}A, \qquad (2)$$

where η is an arbitrary scalar test function, q is the volumetric charge density and ω is the surface charge density, both with respect to the reference configuration. It can be seen that the strong form of the electrostatic weak form in (2) corresponds to Gauss's law.

As the governing field equations in (1) and (2) are decoupled, the electromechanical coupling occurs through the material laws. The hyperelastic material law we adopt here has been utilized in the literature to study the nonlinear deformations of electrostatically actuated polymers; see the works of Vu *et al.*,[35] and Zhao and Suo.[34] Due to the fact that the DE is a rubber-like polymer, phenomenological free energy expressions are typically used to model the deformation of the polymer chains. In the present work, we utilize the form,[34,35]

$$W_{eq}(\boldsymbol{C},\tilde{\boldsymbol{E}}) = \mu W_0 - \frac{1}{2}\lambda(\ln J)^2 - 2\mu W_0(3)\ln J - \frac{\varepsilon}{2}J C_{IJ}^{-1}\tilde{E}_I\tilde{E}_J, \qquad (3)$$

where W_0 is the mechanical free energy density in the absence of an electric field, ε is the permittivity, $\tilde{\boldsymbol{E}}$ is the nominal electric field, $J = \det(\boldsymbol{F})$, where $\boldsymbol{F}$ is the continuum deformation gradient, C_{IJ}^{-1} are the components of the inverse of the right Cauchy–Green tensor $\boldsymbol{C}$, λ is the bulk modulus and μ is the shear modulus. We distinguish the free energy W_{eq} in (3) as the equilibrium free energy as we will define a non-equilibrium free energy that accounts for viscoelastic effects later.

We model the mechanical behavior of the DE using the Arruda–Boyce rubber hyperelastic function.[49] The mechanical free energy W_0 in (3) is approximated by the following truncated series expansion,

$$W_0(I_1) = \frac{1}{2}(I_1 - 3) + \frac{1}{20N}(I_1^2 - 9) + \frac{11}{1050N^2}(I_1^3 - 27) + \frac{19}{7000N^3}(I_1^4 - 81) + \frac{519}{673750N^4}(I_1^5 - 243), \qquad (4)$$

where N is a measure of the cross link density, I_1 is the trace of $\boldsymbol{C}$, and where the Arruda–Boyce model reduces to a Neo-Hookean model if $N \to \infty$. We emphasize that previous experimental studies of Wissler and Mazza[18] have validated the Arruda–Boyce model as being highly accurate for modeling the large deformation of DEs.

Physically, the equilibrium free energy W_{eq} in (3) arises from the representation of an elastomer as a crosslinked network of long flexible chains that consist of a large number of

monomers. Consequently, the crosslinks have a negligible effect on the polarization of the monomers, such that the elastomer can polarize nearly as freely as a polymer melt. As an idealization, we may assume that the dielectric behavior of an elastomer is exactly the same as that of a polymer melt.

Furthermore, in an elastomer, each individual polymer chain has a finite extensibility. In the undeformed state, the polymer chains assumes a coiled configuration, which allows for a large number of conformations. The polymer chains first straighten upon loading. As the loads increase, the end-to-end distance of each polymer chain approaches the finite contour length, and the elastomer approaches a limiting stretch. On approaching the limiting stretch, the elastomer stiffens rapidly, which is captured by the Arruda–Boyce hyperelastic model in (4).

2.1 Finite viscoelasticity

To describe the well-known viscous, or rate effects on the electromechanical behavior and properties of DEs, we applied the finite nonlinear viscoelasticity approach first proposed by Reese and Govindjee.[1] This approach was recently adopted by Hong[38] to develop an analytical model for viscoelastic effects on DEs. We adopt the approach of Reese and Govindjee[1] in the present work because, unlike many existing theories of viscoelasticity,[44,45] it does not restrict the material behavior to small perturbations away from thermodynamic equilibrium (*i.e.* finite linear viscoelasticity), and thus is valid for large viscous deformations, such as creep, or equivalently for large viscous deformation rates. The interested reader may consult Reese and Govindjee,[1] Govindjee and Reese[50] and Nguyen[47] for a detailed discussion distinguishing between finite viscoelasticity and finite linear viscoelasticity.

In the finite nonlinear viscoelasticity theory of Reese and Govindjee,[1] the deformation gradient $\boldsymbol{F}$ is decomposed into elastic and viscous components $\boldsymbol{F} = \boldsymbol{F}^{e}\boldsymbol{F}^{v}$ to describe the time-dependent mechanical response. The free energy is additively decomposed into a time-independent equilibrium part dependent on the total deformation and electric field, and a time-dependent non-equilibrium part dependent on the elastic component of the deformation,

$$W_{\text{total}} = W_{\text{eq}}(\boldsymbol{C},\tilde{\boldsymbol{E}}) + W_{\text{neq}}(\boldsymbol{C}^{e}), \tag{5}$$

where $\boldsymbol{C} = \boldsymbol{F}^{T}\boldsymbol{F}$ and $\boldsymbol{C}^{e} = \boldsymbol{F}^{e^{T}}\boldsymbol{F}^{e}$. The non-equilibrium free energy $W_{\text{neq}}(\boldsymbol{C}^{e})$ is assumed to be independent of the electric field based on the assumption that electrostatic equilibrium occurs much more quickly than mechanical equilibrium.[38]

The constitutive relations for the stress response and evolution equation for the internal deformation are developed using the Coleman and Gurtin[51] thermodynamic theory of internal variables. The 2nd Piola–Kirchhoff stress is defined as,

$$\boldsymbol{S} = 2\frac{\partial W_{\text{eq}}}{\partial \boldsymbol{C}} + \boldsymbol{F}^{v^{-1}}2\frac{\partial W_{\text{neq}}}{\partial \boldsymbol{C}^{e}}\boldsymbol{F}^{v^{-T}}, \tag{6}$$

which results in an additive decomposition of the stress response $\boldsymbol{S} = \boldsymbol{S}_{\text{eq}} + \boldsymbol{S}_{\text{neq}}$. The evolution equation for the internal deformation is restricted to satisfy the positive dissipation criteria. The following evolution equation was proposed by Reese and Govindjee:[1]

$$-\frac{1}{2}\mathscr{L}_{v}\boldsymbol{b}_{e}\cdot\boldsymbol{b}_{e}^{-1} = \mathscr{V}^{-1}\colon \tau_{\text{neq}}, \tag{7}$$

where $\boldsymbol{b}_{e} = \boldsymbol{F}_{e}\cdot\boldsymbol{F}_{e}^{T}$, and where $\mathscr{L}_{v}$ denotes the Lie time derivative, an objective rate, of the elastic component of the deformation tensor. The flow stress τ_{neq} is the non-equilibrium component of the Kirchhoff stress tensor $\tau = \boldsymbol{FSF}^{T}$. The mobility tensor (more commonly known as viscosity tensor) $\mathscr{V}$ must be positive definite to satisfy (7), and takes the following form for an isotropic material,[1]

$$\mathscr{V}^{-1} = \frac{1}{2\eta_{s}}\left(\mathbb{I} - \frac{1}{3}\boldsymbol{I}\otimes\boldsymbol{I}\right) + \frac{1}{9\eta_{b}}\boldsymbol{I}\otimes\boldsymbol{I}, \tag{8}$$

where $\mathbb{I}$ is the fourth order identity tensor, and η_{s} and η_{b} represent the shear and bulk viscosities, respectively. The shear and bulk viscosities are used to derive relaxation times for the viscoelastic DE, and we will investigate the effects of each in a parametric study below.

The additive decomposition of the free energy in (5) is useful for the subsequent numerical developments as the second Piola–Kirchhoff stress and material tangent moduli are needed for the FEM formulation can be decomposed into both equilibrium and non-equilibrium contributions,

$$\mathscr{C} = \mathscr{C}_{\text{eq}} + \mathscr{C}_{\text{neq}} = 4\frac{\partial^{2} W_{\text{eq}}}{\partial \boldsymbol{C}^{2}} + 4\frac{\partial^{2} W_{\text{neq}}}{\partial \boldsymbol{C}^{2}}. \tag{9}$$

The reader is referred to Reese and Govindjee[1] for a detailed derivation of the material tangent modulus for numerical implementation in a finite element formulation.

3 Viscoelastic Q1P0 finite element formulation

3.1 Base viscoelastic finite element formulation

Recently, Park *et al.*[32] developed a nonlinear, finite deformation, dynamic FEM formulation of the governing nonlinear electromechanical field equations of Suo *et al.*[24] that are summarized in (1) and (2). By using a standard FEM approximation to both the mechanical displacement and electric potential, incorporating inertial effects in the mechanical momentum equation, and then obtaining the relevant variational forms of the field equations in (1) and (2), an implicit, coupled, monolithic nonlinear dynamic FEM formulation was obtained with the governing equations,

$$\begin{pmatrix}\Delta\boldsymbol{a}\\ \Delta\Phi\end{pmatrix} = -\begin{pmatrix}\boldsymbol{M} + \beta\Delta t^{2}\boldsymbol{K}_{\text{mm}}^{\text{eq}} & \boldsymbol{K}_{\text{me}}\\ \beta\Delta t^{2}\boldsymbol{K}_{\text{em}} & \boldsymbol{K}_{\text{ee}}\end{pmatrix}^{-1}\begin{pmatrix}\boldsymbol{R}_{\text{mech}}\\ \boldsymbol{R}_{\text{elec}}\end{pmatrix}, \tag{10}$$

where $\boldsymbol{M}$ is the lumped FEM mass matrix, $\Delta\boldsymbol{a}$ is the increment in mechanical acceleration, $\Delta\Phi$ is the increment in electrostatic potential, $\beta = 0.25$ is the standard Newmark time integrator parameter,[52] Δt is the time step, $\boldsymbol{R}_{\text{mech}}$ is the mechanical residual, $\boldsymbol{R}_{\text{elec}}$ is the electrical residual, and the various stiffness matrices $\boldsymbol{K}$ include the purely (equilibrium) mechanical ($\boldsymbol{K}_{\text{mm}}^{\text{eq}}$), mixed electromechanical ($\boldsymbol{K}_{\text{me}} = \boldsymbol{K}_{\text{em}}^{T}$), and purely electrostatic ($\boldsymbol{K}_{\text{ee}}$) contributions. The governing FE equations in (10) are

nonlinear, and thus are solved iteratively until convergence is reached for a given mechanical or electrostatic load increment.

Explicit expressions for the various mechanical, electromechanical, and electrostatic residual vector and stiffness matrices can be found in Park *et al.*[32] This method was shown to capture inhomogeneous electromechanical deformation, including wrinkling, creasing and snap through instabilities that are the common failure modes of DEs. However, it did not include dissipative effects such as viscoelasticity, nor did it address the issue of volumetric locking due to material incompressibility.

Incorporation of the Reese and Govindjee[1] finite nonlinear viscoelasticity formulation into the previous FEM formulation of Park *et al.*[32] is relatively straightforward because of the additive decomposition of the total free energy into equilibrium and non-equilibrium contributions in (5). Moreover, the non-equilibrium free-energy depends only on mechanical fields and deformation. Because of this, when viscoelastic effects are accounted for using the approach of Reese and Govindjee,[1] the original governing dynamic FEM equations in (10) become

$$\begin{pmatrix} \Delta \boldsymbol{a} \\ \Delta \Phi \end{pmatrix} = -\begin{pmatrix} \boldsymbol{M} + \beta \Delta t^2 \boldsymbol{K}_{\mathrm{mm}}^{\mathrm{eq}} + \boldsymbol{K}_{\mathrm{mm}}^{\mathrm{neq}} & \boldsymbol{K}_{\mathrm{me}} \\ \beta \Delta t^2 \boldsymbol{K}_{\mathrm{em}} & \boldsymbol{K}_{\mathrm{ee}} \end{pmatrix}^{-1} \begin{pmatrix} \boldsymbol{R}_{\mathrm{mech}} \\ \boldsymbol{R}_{\mathrm{elec}} \end{pmatrix}. \quad (11)$$

As can be seen by comparing the viscoelastic FEM equations in (11) with the non-viscoelastic equations in (10), the purely equilibrium mechanical contribution to the stiffness matrix is augmented with the non-equilibrium mechanical contribution to the stiffness matrix, which can be written explicitly as

$$\boldsymbol{K}_{\mathrm{mm}}^{\mathrm{neq}} = \int_V \left(2\delta_{\mathrm{ik}} \frac{\partial W_{\mathrm{neq}}(\boldsymbol{C}^{\mathrm{e}})}{\partial C_{\mathrm{JL}}} + 4F_{\mathrm{iM}} F_{\mathrm{kN}} \frac{\partial^2 W_{\mathrm{neq}}(\boldsymbol{C}^{\mathrm{e}})}{\partial C_{\mathrm{JM}} \partial \boldsymbol{C}_{\mathrm{LN}}} \frac{\partial N_{\mathrm{a}}}{\partial X_{\mathrm{J}}} \frac{\partial N_{\mathrm{b}}}{\partial X_{\mathrm{L}}} \right) \mathrm{d}V, \quad (12)$$

where again, the details of the non-equilibrium stresses and moduli that are needed to evaluate $\boldsymbol{K}_{\mathrm{mm}}^{\mathrm{neq}}$ are derived in Reese and Govindjee.[1] We re-emphasize that the additive contribution of the non-equilibrium stiffness matrix $\boldsymbol{K}_{\mathrm{mm}}^{\mathrm{neq}}$ that is seen in (11) is a direct consequence of the additive decomposition of the free energy into equilibrium and non-equilibrium components in (5).

3.2 Q1P0 viscoelastic finite element formulation

The final step needed to complete the locking-resistant, viscoelastic FEM formulation for DEs is to modify the formulation in (11) to alleviate the effects of volumetric locking. The effects of volumetric locking within the context of DEs manifest themselves numerically, as we will demonstrate later in the Appendix, by the prediction of artificially high critical electric fields that are needed to induce electromechanical instabilities. In the FEM context, volumetric locking occurs due to the inability of linear (low-order) FEs to reproduce an isochoric, or volume-preserving deformation. Further insight into FEM techniques to alleviate locking is given in Belytschko *et al.*[53]

We adopt here the seminal approach developed by Simo *et al.*[48] to alleviate the volumetric locking effects. The Simo *et al.*[48] work relies upon a three-field Hu-Washizu variation principle that treats the displacements, pressure and Jacobian as independent variables along with a kinematic split that decomposes the deformation gradient $\boldsymbol{F}$ into deviatoric and volumetric components.

We first introduce the relevant kinematic variables and the kinematic split. Given a motion $\phi(\boldsymbol{X},t)$, we can define the deformation gradient $\boldsymbol{F}$ and Jacobian J as,

$$\boldsymbol{F} = \frac{\partial \phi}{\partial \boldsymbol{X}}, J = \det \boldsymbol{F}. \quad (13)$$

We additionally define,

$$\bar{\boldsymbol{F}} = \Theta^{1/3} \hat{\boldsymbol{F}}, \hat{\boldsymbol{F}} = J^{-1/3} \boldsymbol{F}, \quad (14)$$

where Θ is a new kinematic variable. The key idea underlying the multiplicative split of the deformation gradient into volumetric and deviatoric components is that while in the continuous case $\Theta(\boldsymbol{X},t) = J(\boldsymbol{X},t)$ such that $\bar{\boldsymbol{F}} = \boldsymbol{F}$, this identity does not hold when constructing a discrete, or finite-dimensional approximation. The modified right Cauchy–Green tensor $\boldsymbol{C}$ can now be written as,

$$\boldsymbol{C} = \boldsymbol{F}^{\mathrm{T}} \boldsymbol{F}, \hat{\boldsymbol{C}} = J^{-2/3} \mathrm{C} = \hat{\boldsymbol{F}}^{\mathrm{T}} \hat{\boldsymbol{F}}. \quad (15)$$

Due to the modification of the deformation gradient and Cauchy–Green tensors in (14) and (15), the free energy of the ideal DE in (3) is now written in the form,

$$W = \tilde{W}(\Theta^{2/3} \hat{\boldsymbol{C}}, \tilde{\boldsymbol{E}}), \quad (16)$$

where we note that all resulting modifications to the free energy are to the mechanical kinematic variables, and not the nominal electric field. The corresponding second ($\boldsymbol{S}$) Piola–Kirchhoff stress tensor is then obtained *via*,

$$\bar{\boldsymbol{S}} = \left. \frac{\partial \tilde{W}\left(\boldsymbol{C}, \tilde{\boldsymbol{E}}\right)}{\partial \boldsymbol{C}} \right|_{\boldsymbol{C} = \Theta^{2/3} \hat{\boldsymbol{C}}}. \quad (17)$$

The modified kinematic variables are then utilized in the following Lagrangian:

$$L(\boldsymbol{u}, \Theta, p) = \int_V \overline{W}\left(\Theta^{1/3} \hat{\boldsymbol{F}}\right) \mathrm{d}V + \int_V p(J - \Theta) \mathrm{d}V + \Pi^{\mathrm{ext}}(\boldsymbol{u}) - K(\dot{\boldsymbol{u}}), \quad (18)$$

where $\Pi^{\mathrm{ext}}(\boldsymbol{u})$ is the external work due to body forces and prescribed tractions, and $K(\dot{\boldsymbol{u}})$ is the kinetic energy. It is clear that the purpose of the pressure p in (18) is to enforce the incompressibility condition in the discrete formulation, *i.e.* $J = \Theta$. Furthermore, as shown by Simo *et al.*,[48] the pressure p is eliminated at the element level such that the resulting FEM equations include only the standard displacement (or acceleration) nodal degrees of freedom.

In deriving the governing FEM equations, a mixed projection approach was utilized by Simo *et al.*[48] The mixed approximation arises because while the nodal displacement field is interpolated using standard, linear FEM shape functions, the element-level pressure and volume are approximated using a lower order, constant approximation, thus resulting in the Q1P0

moniker. The projection arises because the shape function gradients $\boldsymbol{B}$ are decomposed into volumetric and deviatoric components, where the deviatoric components are calculated from the gradients of the shape functions but the volumetric components are approximated by the mean dilation component for the element to provide a lower order constant approximation for the volumetric deformation and pressure. Specifically,

$$\bar{\boldsymbol{B}}^{\mathrm{I}} = \boldsymbol{B}^{\mathrm{I}}_{\mathrm{dev}} + \bar{\boldsymbol{B}}^{\mathrm{I}}_{\mathrm{vol}}, \tag{19}$$

where the explicit expressions for the $\bar{\boldsymbol{B}}$ shape function gradients can be found in Hughes.[52]

Coupling the Q1P0 formulation of Simo *et al.*[48] in (18) with the electromechanical field equations of Suo *et al.*[24] in (1) and (2) and the standard FE approximation to the mechanical displacement and electrostatic potential, we arrive at the following FEM governing equation that incorporates the finite viscoelasticity approach of Reese and Govindjee[1] and also the locking-resistant Q1P0 formulation of Simo *et al.*:[48]

$$\begin{pmatrix} \Delta \boldsymbol{a} \\ \Delta \Phi \end{pmatrix} = -\begin{pmatrix} \boldsymbol{M} + \beta \Delta t^2 \boldsymbol{K}^{\mathrm{eq}}_{\mathrm{mm+q1p0}} + \boldsymbol{K}^{\mathrm{neq}}_{\mathrm{mm}} & \boldsymbol{K}_{\mathrm{me}} \\ \beta \Delta t^2 \boldsymbol{K}_{\mathrm{em}} & \boldsymbol{K}_{\mathrm{ee}} \end{pmatrix}^{-1} \begin{pmatrix} \boldsymbol{R}_{\mathrm{mech}} \\ \boldsymbol{R}_{\mathrm{elec}} \end{pmatrix}. \tag{20}$$

Incorporation of the Q1P0 formulation of Simo *et al.*[48] results in some modifications to the various terms in (20). First, the internal mechanical force is modified as

$$\boldsymbol{f}^{\mathrm{int}}_{\mathrm{m}} = \int_V \overline{\boldsymbol{B}}^{\mathrm{T}} \left(\frac{1}{J} \boldsymbol{F} \overline{\boldsymbol{S}} \boldsymbol{F}^{\mathrm{T}} \right) \mathrm{d}v \Big|_{\boldsymbol{F} = \Theta^{1/3} \hat{\boldsymbol{F}}}. \tag{21}$$

Second, because the electromechanical stiffness matrices are derived from a linearization of the modified internal mechanical force in (21), it becomes

$$\boldsymbol{K}_{\mathrm{me}} = \frac{\partial \boldsymbol{f}^{\mathrm{int}}_{\mathrm{m}}}{\partial \bar{\boldsymbol{E}}} = \int_V \overline{\boldsymbol{B}}^{\mathrm{T}} \left(\frac{1}{J} \boldsymbol{F} \frac{\partial \overline{\boldsymbol{S}}}{\partial \bar{\boldsymbol{E}}} \boldsymbol{F}^{\mathrm{T}} \right) \boldsymbol{B} \mathrm{d}v \Big|_{\boldsymbol{F} = \Theta^{1/3} \hat{\boldsymbol{F}}}, \tag{22}$$

where it is clear that the electromechanical stiffness in (22) has become mixed in the sense that it depends on both the standard FE shape function gradients as well as the modified $\bar{\boldsymbol{B}}$ shape function gradients.

Finally, as noted by Simo *et al.*,[48] the mechanical stiffness matrices $\boldsymbol{K}^{\mathrm{eq}}_{\mathrm{mm+q1p0}}$ in (20) can be written

$$\boldsymbol{K}^{\mathrm{eq}}_{\mathrm{mm+q1p0}} = \boldsymbol{K}_{\mathrm{geo}} + \boldsymbol{K}_{\mathrm{mat}} + \boldsymbol{K}_{\mathrm{p}}, \tag{23}$$

where $\boldsymbol{K}_{\mathrm{geo}}$ and $\boldsymbol{K}_{\mathrm{mat}}$ are the standard geometric and material contributions to the stiffness matrix, and where $\boldsymbol{K}_{\mathrm{p}}$ is a new contribution to the stiffness matrix that emerges due to the incompressibility pressure constraint in (18). We evaluate the stresses and moduli that are needed in (23) for the equilibrium ($\boldsymbol{K}^{\mathrm{eq}}_{\mathrm{mm+q1p0}}$) tangent stiffness in (20) using the numerical finite difference approach of Miche.[54]

4 Numerical results

4.1 Homogeneous deformation: single relaxation time

We first examine how viscoelasticity impacts the electromechanical behavior of DEs under homogeneous deformation. The model DE geometry was a cube of side length one that is traction and mechanical constraint-free and thus effectively free-standing. Electrostatic loading was applied through a monotonically increasing charge on the $+y$ surface, while the $-y$ surface was prescribed a constant (zero) voltage. The material constants for the DE were set as (see eqn (3) and (4)): $\mu = \varepsilon = 1$, $\lambda = 10000$, $N = 5.0$. These parameters were chosen as they enable the DE to undergo an electromechanical instability *via* softening in the normalized voltage *vs.* charge curve,[33] while the ratio $\lambda/\mu = 10000$ was used to enforce incompressibility of the DE. The parameters for the shear and bulk relaxation times τ_{s} and τ_{b} were varied as well as the loading rate to evaluate the effect of deviatoric and volumetric viscoelasticity. All calculations were performed in 3D with a single 8-node hexahedral finite element using the Sandia-developed simulation code Tahoe.[55] The FE time step chosen was several orders of magnitude smaller than the smallest relaxation time such that the viscoelastic behavior was accurately resolved. In the present work, for simplicity, we assumed that the non-equilibrium free energy takes a Neo-Hookean form.

4.1.1 Shear and bulk time constant effects. We first examined the effects of varying either the bulk or shear relaxation time, while holding the other one fixed, with the results for varying the shear relaxation time summarized in Fig. 1. These numerical examples are thus based upon a single relaxation time in either the bulk or shear mode, and will be contrasted with the multiple relaxation time cases discussed below. The shear and bulk relaxation times τ_{s} and τ_{b} have all been normalized in this and subsequent figures by multiplying the relaxation time by the loading rate. For the case shown in Fig. 1, the bulk relaxation time was held fixed at a very small value relative to the shear relaxation times to enable us to delineate the effect of varying the shear relaxation time. We will demonstrate in a later discussion that having the bulk relaxation time be comparable to the shear relaxation time does not change the conclusions we reach based on the results in Fig. 1.

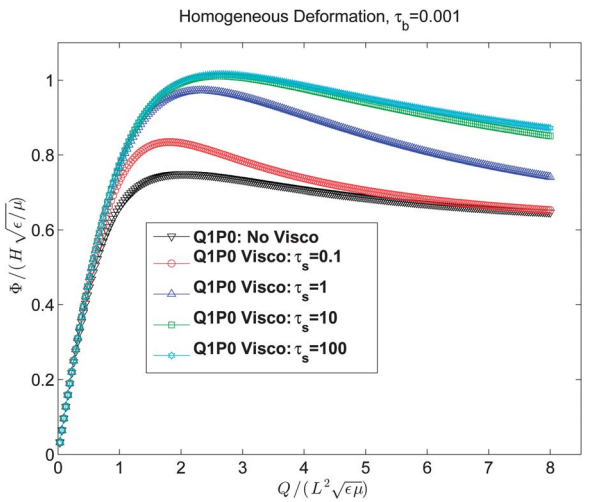

Fig. 1 Effects of varying τ_{s} on the electromechanical behavior of DEs undergoing homogeneous deformation.

Our first result, though not shown pictorially, was obtained by keeping the shear relaxation time fixed at a small value $\tau_s = 0.001$, while varying the bulk relaxation time τ_b. However, we found that varying τ_b four orders of magnitude[56] does not lead to any difference in the electromechanical behavior of the DE, which exhibits an initial increase in the normalized voltage–charge curve, followed by electromechanical instability occurring at a normalized voltage of about $\Phi = 0.75$ (see, for example, the black curve in Fig. 1). The likely reason for the fact that the bulk relaxation time has little effect is due to the incompressible behavior of DEs, where there is no appreciable volumetric deformation.

In contrast, if $\tau_b = 0.001$ and τ_s is varied over three orders of magnitude as shown in Fig. 1, the critical voltage and charge needed to induce the electromechanical instability gradually increase as compared to the case in which viscoelastic effects are neglected. We see that when $\tau_s = 10$, the critical voltage to induce the electromechanical instability increases about 36% from 0.75 to 1.02. However, it is also observed that increasing the single shear relaxation time τ_s above 10 does not appear to appreciably change either the critical voltage for instability, nor the resulting post-instability behavior. This result suggests that, as predicted previously by Zhao *et al.*,[39] viscous effects delay the onset of electromechanical instabilities in DEs.

As demonstrated in Fig. 1, time-dependent behavior is observed for a narrow range of relaxation times, *i.e.* $0.1 < \tau_s < 10$. For $\tau_s < 0.1$, the loading rate is significantly lower than the relaxation rate such that the material remains in equilibrium throughout the deformation. For $\tau_s > 10$, the loading rate is significantly faster than the relaxation rate such that there is insufficient time for appreciable relaxation of the material to occur during deformation. At equilibrium, the shear modulus is the same as the shear modulus μ for the elastic (no viscoelastic) case, thus the instability behavior of the two cases are identical. The shear modulus of the unrelaxed material is 2μ, which by the scaling analysis done in Fig. 1 where both the charge Q and voltage Φ are normalized by $\sqrt{\varepsilon/\mu}$, indicates that the breakdown voltage should increase by about a factor of $\sqrt{2}$, or 41%. This is in fact very close to the 36% increase observed in Fig. 1 for the $\tau_s = 100$ case. Larger normalized relaxation times would have no further effect on the dielectric behavior.

To further demonstrate the relative importance of τ_s as compared to τ_b, we show in Fig. 2 the normalized voltage–charge curves if $\tau_s = \tau_b$ for a range of values spanning three orders of magnitude. It is clearly seen that Fig. 2 is quite similar to Fig. 1b in which $\tau_b = 0.001$ and τ_s is varied, which again suggests that the bulk relaxation time τ_b does not strongly impact the electromechanical behavior of DEs, particularly in comparison to the shear relaxation time τ_s.

4.1.2 Loading rate effects. Another important parameter to consider within the context of viscoelasticity is the effect of electrical loading rate on the electromechanical behavior of the DEs. We illustrate this effect in Fig. 3, again for the case of homogeneous deformation of a free-standing film.

Of interest, the results in Fig. 3 nearly identical to those seen in Fig. 1b for when the shear time constant was varied. This is because the normalized time constant τ_s we plot is the shear

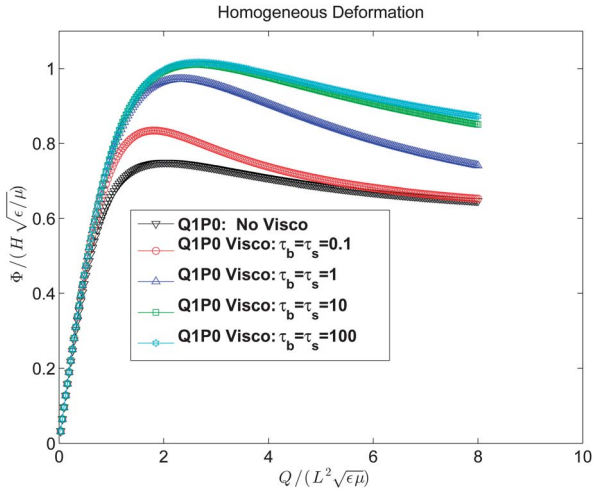

Fig. 2 Normalized voltage–charge curves for a DE undergoing homogeneous deformation if $\tau_s = \tau_b$.

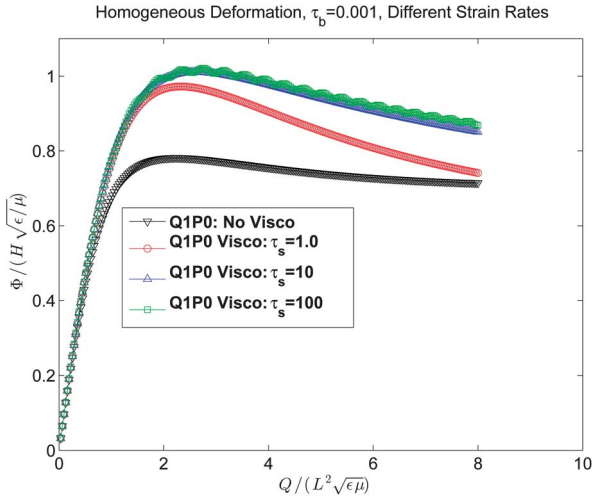

Fig. 3 Effect of different charge loading rates on the electromechanical behavior of viscoelastic DEs undergoing homogeneous deformation.

viscosity multiplied by the loading rate. Therefore, even if the shear viscosity η_s is kept constant, the normalized time constant τ_s increases due to the increase in loading rate, and thus we find that regardless how the time constant is decomposed (*i.e.* lower viscosity and higher loading rates *vs.* higher viscosity and lower loading rates), the net electromechanical behavior appears to be quite similar for the same normalized τ_s.

4.2 Homogeneous deformation: multiple relaxation times

We continue our study of the free-standing film model problem by examining the effect of a distribution of relaxation times on the electromechanical behavior of DEs. We again choose a very small bulk relaxation time of $\tau_b = 0.001$, and focus on the effect of multiple shear relaxation times τ_s. In enabling a distribution of shear relaxation times, we constrain the non-equilibrium potentials such that $1 + \sum_{i=1}^{N} \mu_{neq_i}/\mu_{eq}$ is the same for a different number of non-equilibrium processes N. This is done to ensure

that the stiffness of the instantaneous response of the DE is not changed by having multiple relaxation times and non-equilibrium potentials. Fig. 4 demonstrates this for two such ratios, where $\sum\mu_{neq} = 1$ and $\sum\mu_{neq} = 10$. The μ_{neq} was the sum divided by the number of non-equilibrium processes. For example, if $\sum\mu_{neq} = 10$, and there were 4 non-equilibrium processes, then each non-equilibrium process had a $\mu_{neq} = 2.5$.

We show in Fig. 4 the results of choosing shear relaxation times with a wider and higher range, up to five orders of magnitude. The results suggest that a system with the distribution of shear relaxation times requires more electrostatic loading in order to exhibit the electromechanical instability. The post-instability behavior, however, appears to depend on the values of the non-equilibrium shear moduli μ_{neq}.

The values of the non-equilibrium shear moduli appear to have a significant effect on the critical electric field for electromechanical instability. While an increase in the critical electric field of about 29% is observed when $1 + \sum\mu_{neq}/\mu_{eq} = 2$, the increase is about 2.7 times the no viscoelasticity result when five relaxation orders of relaxation times are present, and when $1 + \sum\mu_{neq}/\mu_{eq} = 11$. Performing the same scaling analysis as above for the single relaxation time case, we can compare the increase in the critical voltage needed to induce electromechanical instability that is obtained from the FEM calculation to that predicted analytically. For the $\sum\mu_{neq} = 1$ case, if five orders of relaxation times are considered, the increase in the critical voltage in Fig. 4a reaches 91% of the predicted enhancement. For the $\sum\mu_{neq} = 10$ case for five relaxation times in Fig. 4b, 81% of the predicted enhancement in the critical voltage is reached.

The results in Fig. 4b demonstrate that the impact of viscoelastic effects depends on the breadth of the relaxation spectrum. For a given loading rate, viscoelastic behavior characterized by a broader relaxation spectrum (more non-equilibrium processes) requires progressively higher critical voltage to induce electromechanical instability. Elastomeric materials exhibit a very broad relaxation spectrum, spanning multiple orders of magnitude in time. It is also worth noting the gradual decrease in voltage after the onset of electromechanical instability seen in Fig. 4b. This gradual relaxation will have a significant impact on the crack propagation speeds observed in the numerical example on bursting drops in quasi-3D dielectric solids.

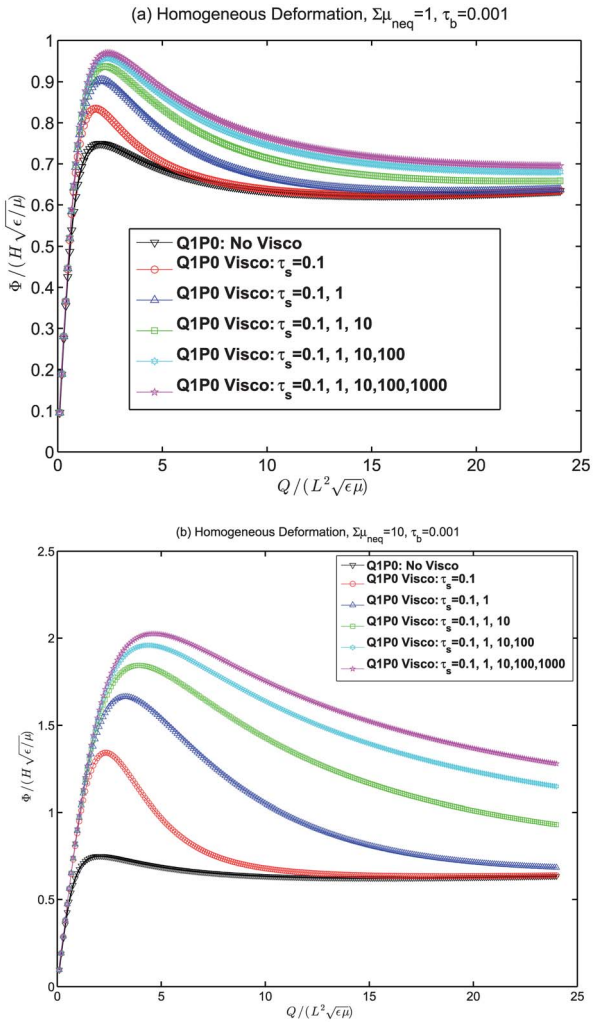

Fig. 4 Effects of a distribution of shear relaxation times τ_s on the electromechanical behavior of DEs undergoing homogeneous deformation. (a) $1 + (\sum\mu_{neq})/\mu_{eq} = 2$. (b) $1 + (\sum\mu_{neq})/\mu_{eq} = 11$.

4.3 Charge-induced creep: single and multiple relaxation times

To provide further insight into the effects of the different shear relaxation times on the viscoelastic response of DEs, we perform an electromechanical analog of the classical creep test in which the freestanding DE is subject to a constant charge load, while the resulting in-plane and out-of-plane stretches λ are monitored as a function of time, as shown in Fig. 5 for $\mu_{neq} = 10$. As seen in Fig. 5, both in and out-of-plane stretches converge to a limiting value as time increases, with the convergence time being strongly correlated to the shear relaxation time τ_s. The oscillatory nature of the stretches arises due to the presence of dynamic wave propagation, though the magnitude of the oscillations is correctly observed to decrease with increasing time, while also eventually oscillating (correctly) about the converged value of stretch.

We also discuss the creep response if multiple relaxation times are active in Fig. 6, for the $1 + \sum\mu_{neq}/\mu_{eq} = 11$ case, where the creep response is again obtained by applying a constant charge on the freestanding DE. In particular, Fig. 6 demonstrates the substantial, order of magnitude variations in the time taken to relax to the final state of deformation if a wide spectrum of relaxation times are active. We also note that, in comparing the relaxation to the converged stretch in Fig. 5 and 6, the relaxation times are slightly faster for the multiprocess case in Fig. 6. This is because the relaxation is distributed over a broad range of relaxation times rather than a single relaxation time.

4.4 Bursting drops in a quasi-plane strain dielectric solids

We focus our large-scale numerical investigation of viscoelastic effects on electromechanical instabilities in DEs on recent experiments performed by Wang *et al.*[23] The experimental configuration is shown in Fig. 7a. The problem is one of a dielectric film with a small hole containing a conductive liquid,

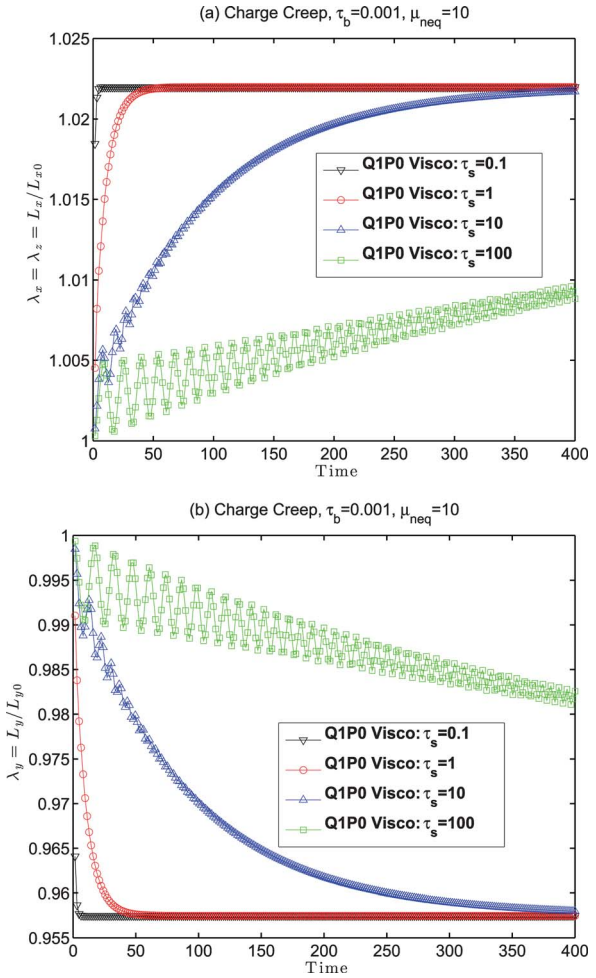

Fig. 5 Charge creep-induced relaxation of (a) in-plane ($\lambda_x = \lambda_z$) and (b) out-of-plane λ_y stretch as a function of time for a range of individual shear relaxation times, for $\mu_{neq} = 10$.

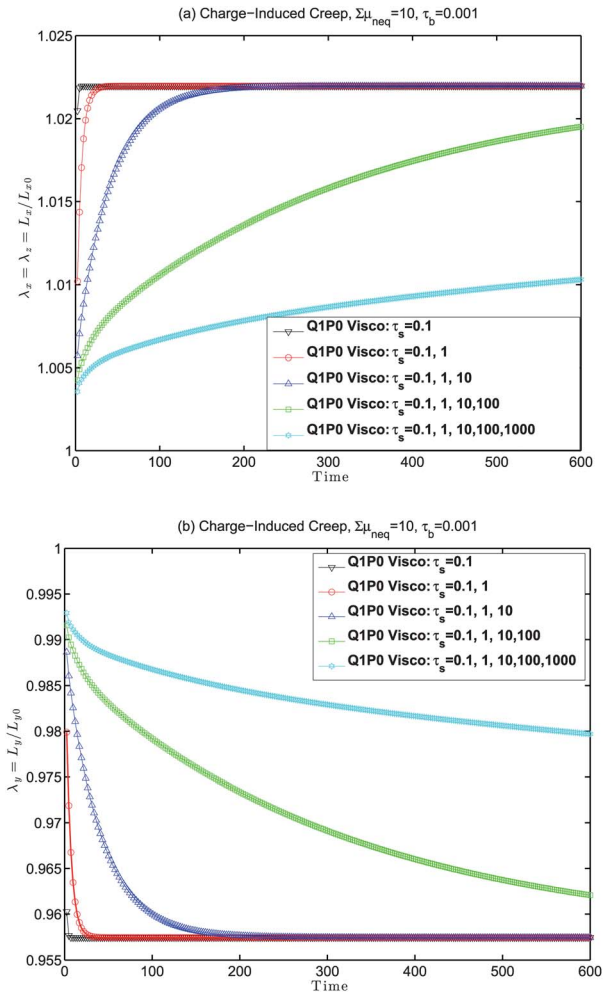

Fig. 6 Charge creep-induced relaxation of (a) in-plane ($\lambda_x = \lambda_z$) and (b) out-of-plane (λ_y) stretch as a function of time for multiple shear relaxation times τ_s where $1 + (\sum\mu_{neq})/\mu_{eq} = 11$.

for example NaCl solution. All edges of the film are constrained mechanically, and a voltage differential Φ is applied across the film. The novel experimental finding was the first observation of instabilities of drops in solids, in which a different scaling was observed as compared to instabilities of drops in liquids.

We perform a computational study of the experimental work of Wang *et al.*[23] using the one quarter computational model shown in Fig. 7b that exploits the symmetries present in Fig. 7a. Aside from the computational model, another important distinction is that we considered a quasi-plane strain model, rather than the full three-dimensional experiment performed by Wang *et al.*[23] We did this by using the full three-dimensional viscoelastic Q1P0 DEFEM formulation presented in this work, though modeling the film to be only a single element thick, and prescribing all out of plane (z) displacements to be zero. This approximation was done mainly due to significant computational expense for the full three-dimensional model, and also because the critical physics of interest can, as we will demonstrate below, be captured using the quasi-plane strain model. It is noted that an axisymmetric computational model would be an ideal choice for this problem.

The full quasi-plane strain model in Fig. 7b had dimensions of 40 × 40, with the radius of the hole being 2. Therefore, the axisymmetric model had dimensions 20 × 20, with the same hole radius of 2. This axisymmetric geometry was modeled using standard 8-node hexahedral finite elements with a mesh spacing of 0.5, for a total number of 1586 elements and 3332 nodes. We note that the mesh density of 0.5 likely will not result in converged results for the critical electric field, as experience has shown[57] that a finer mesh is needed to obtain quantitative accuracy as compared to experimental and theoretical predictions when using the Q1P0 formulation of Simo *et al.*[48] However, because we have chosen the same mesh density for both viscoelastic and non-viscoelastic simulations, we can achieve the more important result of comparing the effects of viscoelasticity for a fixed mesh density.

We first describe the electromechanical instability and phenomena of interest, as shown by the FEM simulation results in Fig. 8. As seen in Fig. 8a, the circular bubble is initially undeformed prior to application of electrostatic loading. At a critical value of the far-field electric field that is applied to the top of the DE film, as shown in Fig. 7, a sharp crack-like tip

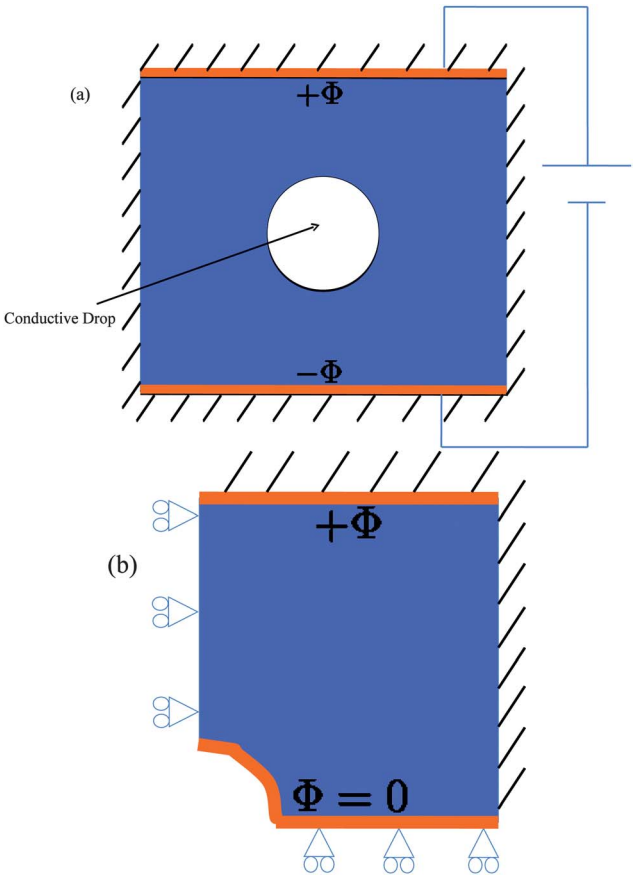

Fig. 7 (a) Experimental and (b) quarter axisymmetric computational models for bursting drop in a dielectric solid based on experiments of Wang *et al.*[23]

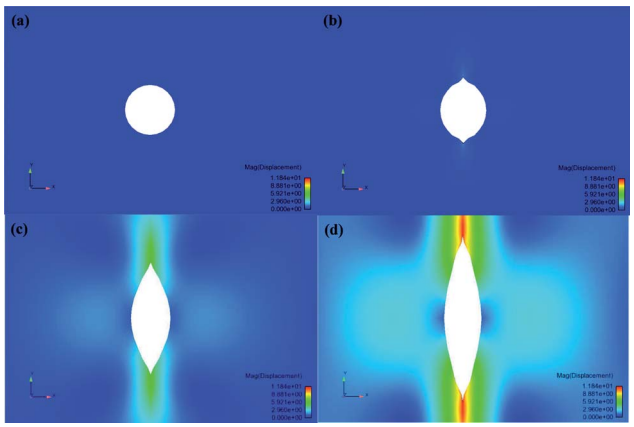

Fig. 8 Representative snapshots of crack propagation in constrained DE film. (a) Initial, undeformed configuration; (b) formation of sharp crack tip at top of the bubble; (c) propagation of crack and elongation of initially circular bubble; (d) further crack propagation and elongation of initially circular bubble. This image is for five orders of relaxation times when $\sum\mu_{neq} = 10$.

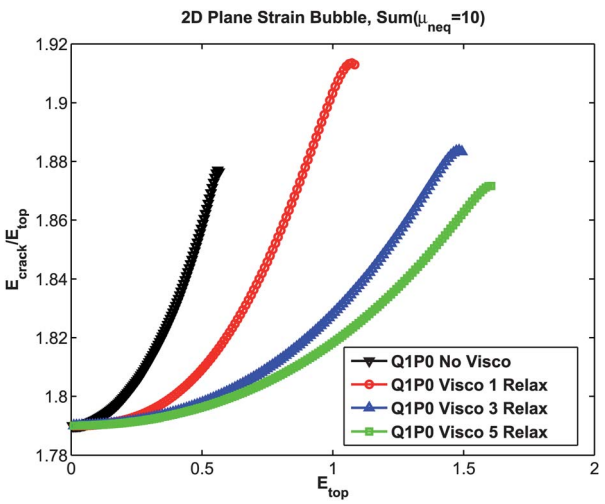

Fig. 9 Electric field at bubble crack tip normalized by far field applied electric field E_{top} for $\sum\mu_{neq} = 10$.

forms at the top of the circular bubble, as shown in Fig. 8b. Further increase of the voltage causes the sharp crack-like feature to propagate vertically towards the applied far-field electrostatic loading, which also causes a distortion of the initially circular bubble into a shape resembling an elongated ellipsoid. Fig. 8d demonstrates further distortion of the circular bubble and crack propagation with increased electrostatic loading. We emphasize that all of these phenomena, *i.e.* the initial sharp crack followed by the vertical propagation of the crack and transformation of the initially circular hole to an elongated ellipsoid, were observed in the full three-dimensional experiments of Wang *et al.*[23]

The critical electric field to initiate the sharp crack was found analytically and experimentally for the three-dimensional bubble by Wang *et al.*[23] to be between $0.55\sqrt{\mu/\varepsilon}$ and $0.6\sqrt{\mu/\varepsilon}$. For our two-dimensional circular bubble without viscoelasticity as shown in Fig. 9, the critical normalized electric field is found to be $E_c = 0.56$, which agrees fortuitously with the three-dimensional bubble results of Wang *et al.*[23] The result is fortuitous because of the relatively coarse FEM mesh size utilized, where refinement of the mesh would lead to convergence of the critical electric field, which should be different in two-dimensions as compared to the three-dimensional experiments of Wang *et al.*[23] However, again, our emphasis in the present work is in capturing the macroscopic phenomena of crack propagation, and comparing the results with and without viscoelasticity for a fixed FEM mesh density. Fig. 9 also demonstrates that the critical electric field at the top of the bubble prior to crack tip nucleation and propagation is nearly two times the applied far field value, which is in agreement with the analytic solution of Kusne and Lamberth.[58]

Fig. 9 also demonstrates the effects of viscoelasticity on the critical electric field E_c, where if $\sum\mu_{neq} = 10$, E_c increases from 0.56 for the no viscoelasticity case to about 1.6 if five decades of relaxation times are active. This result is again consistent with previous analytical studies[39] that viscoelasticity results in higher critical electric fields to cause electromechanical instabilities.

Another important consideration is the effective crack propagation speed if viscoelastic effects become important. We illustrate these effects in Fig. 10, where we plot the normalized deformation of the crack tip as a function of the applied far-field electric field magnitude $\boldsymbol{E}$. Fig. 10 demonstrates that the increase in critical electric field magnitude as well as the crack

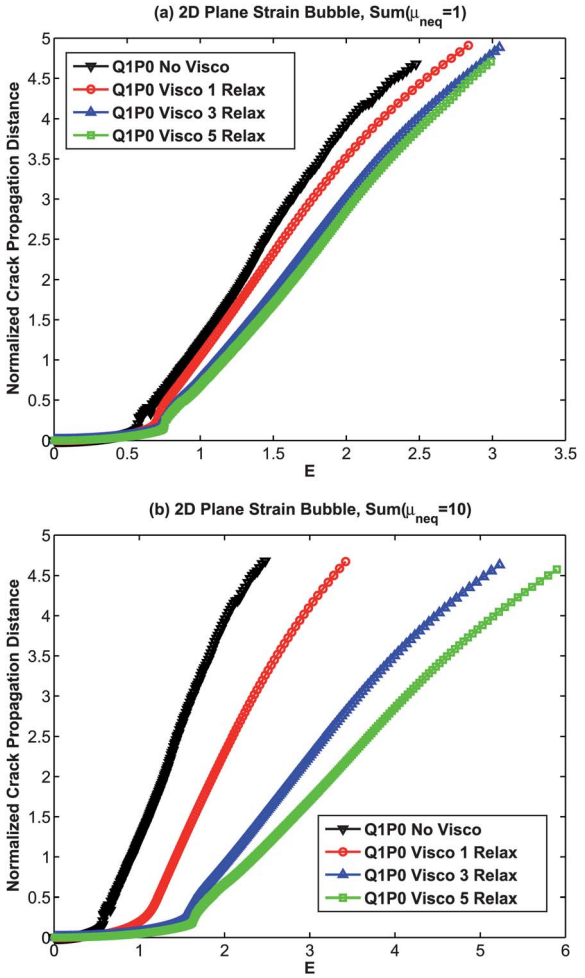

Fig. 10 Effects of multiple shear relaxation times τ_s on the electrostatically induced instability and subsequent crack propagation in constrained quasi-3D DE film. (a) $1 + (\sum \mu_{neq})/\mu_{eq} = 2$. (b) $1 + (\sum \mu_{neq})/\mu_{eq} = 11$.

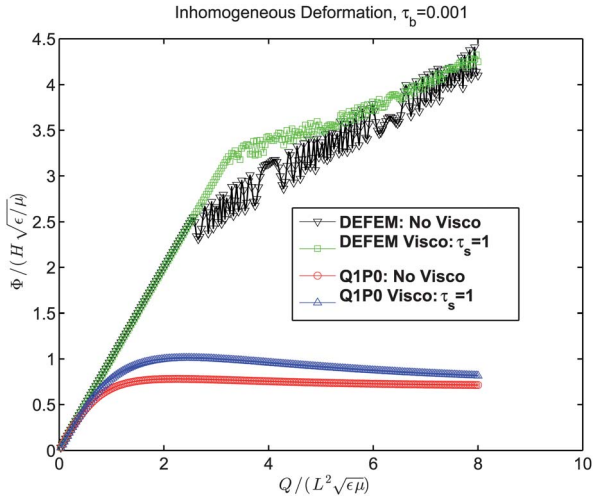

Fig. 11 Effects of not relieving, through the proposed Q1P0 formulation, volumetric locking on the electromechanical behavior of viscoelastic DEs undergoing inhomogeneous deformation.

speed strongly depends not only on the range of relaxation times that are active, but also on the non-equilibrium moduli. The crack tip position was obtained by tracking the displacement of the FE node whose position coincided with the top of the bubble in Fig. 7.

For example, for the case in Fig. 10a where $\sum \mu_{neq} = 1$, indicating that the non-equilibrium shear modulus is comparable to the equilibrium shear modulus, a slight increase in critical electric field is observed if five decades of relaxation times are active. However, the effective crack propagation velocity appears to be little changed compared to the non-viscoelasticity case.

The situation is quite different for the case when $\sum \mu_{neq} = 10$, as shown in Fig. 10b. In that case, not only is the critical electric field increased substantially as previously discussed, but there is a clear decrease in crack speed as a wider range of relaxation times are considered. The viscous energy dissipation rate scales with the non-equilibrium modulus and strain rate, thus slower propagation speeds are expected in a material with a higher non-equilibrium modulus for the same applied work.[59] For example, if a single relaxation time is activated, the crack propagation speed drops to about 78% of the non-viscoelastic crack propagation speed. The results are much more dramatic if the distribution of relaxation times spanned three and five orders of magnitude. For the three orders of magnitude case, the crack propagation speed drops to about 47% of the non-viscoelastic case, while for the five orders of magnitude case, the crack propagation speed drops to 40% of the non-viscoelastic case. The substantial decrease in the crack speed with the breadth of the spectrum of relaxation times can be related to the much more gradual relaxation after electromechanical instability previously observed in Fig. 4b, where the additional stiffening that occurs over a wide range of time scales acts to substantially impede the crack speed that is observed.

5 Conclusions

We have presented a new dynamic, finite deformation finite element model of dielectric elastomers that incorporates finite viscoelasticity, and also alleviates volumetric locking due to material incompressibility. Our single element tests demonstrated the effects that viscoelasticity in the shear properties can have not only on the critical electric fields needed to induce electromechanical instability, but also in the post-instability behavior of the elastomer, where the magnitude of these effects increased with the distribution of shear relaxation times. In contrast, viscoelasticity in the mechanical bulk properties had little effect on the electromechanical behavior.

Our large scale finite element simulations of electromechanical instability, and specifically crack propagation resulting in constrained dielectric elastomer films containing a conductive bubble, illustrated the effects of viscoelasticity in reducing the crack speeds that are observed. This result is similar to that observed in a purely mechanical viscoelastic crack propagation.[59] Overall, our results demonstrate the significant effects of viscoelasticity on dielectric behavior of elastomers undergoing electromechanical instabilities.

6 Appendix

Because we have not quantified the effects of not eliminating volumetric locking, we demonstrate in this Appendix the effects of not relieving volumetric locking through the Q1P0 formulation on the electromechanical behavior of viscoelastic DEs subject to mechanical constraints. The constraints are needed as volumetric locking is not observed for the homogeneous deformation cases corresponding to the freestanding DEs. To constrain the DE, which was a cube of unit length that was discretized by a single 8-node hexahedral finite element, we fixed the $-y$ surface from moving in any direction.

As can be seen in Fig. 11, if volumetric locking effects are not alleviated, the critical normalized voltage and charge needed to induce electromechanical instability is significantly and artificially enhanced as compared to the Q1P0 cases, both with and without rate-dependent material effects. Particularly noteworthy is the fact that the critical normalized voltage is more than three times the critical value if the Q1P0 formulation is not utilized. Furthermore, if volumetric locking is not alleviated, the voltage–charge curve does not exhibit a softening instability. This example is important as it shows that, for the multi-dimensional electromechanical instabilities that we analyzed in Section 4.4, if the volumetric locking effects are not alleviated, that the numerical model will predict an artificially high critical electric field that is needed for the onset of electromechanical instabilities in constrained DE films.

Acknowledgements

HSP acknowledges startup funding from Boston University in support of this research. HSP also acknowledges Prof. Xuanhe Zhao for sharing his experimental data on the bursting drops in solids problem.

References

1 S. Reese and S. Govindjee, *Int. J. Solids Struct.*, 1998, **35**, 3455–3482.
2 F. Carpi, S. Bauer and D. D. Rossi, *Science*, 2010, **330**, 1759–1761.
3 P. Brochu and Q. Pei, *Macromol. Rapid Commun.*, 2010, **31**, 10–36.
4 E. Biddiss and T. Chau, *Med. Eng. Phys.*, 2008, **30**, 403–418.
5 C. Keplinger, T. Li, R. Baumgartner, Z. Suo and S. Bauer, *Soft Matter*, 2012, **8**, 285–288.
6 T. Mirfakhrai, J. D. W. Madden and R. H. Baughman, *Mater. Today*, 2007, **10**, 30–38.
7 R. E. Pelrine, R. D. Kornbluh and J. P. Joseph, *Sens. Actuators, A*, 1998, **64**, 77–85.
8 R. Pelrine, R. Kornbluh, Q. Pei and J. Joseph, *Science*, 2000, **287**, 836–839.
9 J. W. Fox and N. C. Goulbourne, *J. Mech. Phys. Solids*, 2008, **56**, 2669–2686.
10 C. Keplinger, M. Kaltenbrunner, N. Arnold and S. Bauer, *Proc. Natl. Acad. Sci. U. S. A.*, 2010, **107**, 4505–4510.
11 G. Kofod, P. Sommer-Larsen, R. Kornbluh and R. Pelrine, *J. Intell. Mater. Syst. Struct.*, 2003, **14**, 787–793.
12 G. Kofod and P. Sommer-Larsen, *Sens. Actuators, A*, 2005, **122**, 273–283.
13 Q. Pei, R. Pelrine, M. Rosenthal, S. Stanford, H. Prahlad and R. Kornbluh, *Proc. SPIE*, 2004, **5385**, 41–50.
14 J.-S. Plante and S. Dubowsky, *Int. J. Solids Struct.*, 2006, **43**, 7727–7751.
15 J.-S. Plante and S. Dubowsky, *Sens. Actuators, A*, 2007, **137**, 96–109.
16 J.-S. Plante and S. Dubowsky, *Smart Mater. Struct.*, 2007, **16**, S227–S236.
17 H. F. Schlaak, M. Jungmann, M. Matysek and P. Lotz, *Proc. SPIE*, 2005, **5759**, 121–133.
18 M. Wissler and E. Mazza, *Sens. Actuators, A*, 2007, **134**, 494–504.
19 X. Q. Zhang, M. Wissler, B. Jaehne, R. Broennimann and G. Kovacs, *Proc. SPIE*, 2004, **5385**, 78–86.
20 S. Chiba, M. Waki, R. Kornbluh and R. Pelrine, *Proc. SPIE*, 2008, **6927**, 692715.
21 Q. Wang, L. Zhang and X. Zhao, *Phys. Rev. Lett.*, 2011, **106**, 118301.
22 Q. Wang, M. Tahir, L. Zhang and X. Zhao, *Soft Matter*, 2011, **7**, 6583–6589.
23 Q. Wang, Z. Suo and X. Zhao, *Nat. Commun.*, 2012, **3**, 1157.
24 Z. Suo, X. Zhao and W. H. Greene, *J. Mech. Phys. Solids*, 2008, **56**, 467–486.
25 Z. Suo, *Acta Mech. Solida Sin.*, 2010, **23**, 549–578.
26 N. C. Goulbourne, E. M. Mockensturm and M. I. Frecker, *J. Appl. Mech.*, 2005, **72**, 899–906.
27 A. Dorfmann and R. W. Ogden, *Acta Mech.*, 2005, **82**, 99–127.
28 A. Dorfmann and R. W. Ogden, *J. Elasticity*, 2006, **174**, 167–183.
29 R. M. McMeeking and C. M. Landis, *J. Appl. Mech.*, 2005, **72**, 581–590.
30 L. Patrick, K. Gabor and M. Silvain, *Sens. Actuators, A*, 2007, **135**, 748–757.
31 M. Wissler and E. Mazza, *Smart Mater. Struct.*, 2005, **14**, 1396–1402.
32 H. S. Park, Z. Suo, J. Zhou and P. A. Klein, *Int. J. Solids Struct.*, 2012, **49**, 2187–2194.
33 J. Zhou, W. Hong, X. Zhao, Z. Zhang and Z. Suo, *Int. J. Solids Struct.*, 2008, **45**, 3739–3750.
34 X. Zhao and Z. Suo, *Appl. Phys. Lett.*, 2007, **91**, 061921.
35 D. K. Vu, P. Steinmann and G. Possart, *Int. J. Numer. Meth. Eng.*, 2007, **70**, 685–704.
36 W. Li and C. M. Landis, *Smart Mater. Struct.*, 2012, **21**, 094006.
37 C. Keplinger, M. Kaltenbrunner, N. Arnold and S. Bauer, *Appl. Phys. Lett.*, 2008, **92**, 192903.
38 W. Hong, *J. Mech. Phys. Solids*, 2011, **59**, 637–650.
39 X. Zhao, S. J. A. Koh and Z. Suo, *J. Appl. Mech.*, 2011, **3**, 203–217.
40 C. C. Foo, S. Cai, S. J. A. Koh, S. Bauer and Z. Suo, *J. Appl. Phys.*, 2012, **111**, 034102.
41 J. D. Ferry, *Viscoelastic Properties of Polymers*, John Wiley and Sons, New York, NY, 1980.

42 R. S. Lakes, *Viscoelastic Solids*, CRC Press, Boca Raton, FL, 1999.
43 E. Yang, M. Frecker and E. Mockensturm, *Proc. SPIE*, 2005, **5759**, 82–93.
44 J. C. Simo, *Comput. Meth. Appl. Mech. Eng.*, 1987, **60**, 153–173.
45 G. A. Holzapfel, *Int. J. Numer. Meth. Eng.*, 1996, **39**, 3903–3926.
46 S. Govindjee and S. Reese, *J. Eng. Mater. Technol.*, 1997, **119**, 251–255.
47 T. D. Nguyen, *Proceedings of the IUTAM Symposium on Cellular, Molecular and Tissue Mechanics*, 2010, pp. 55–65.
48 J. C. Simo, R. L. Taylor and K. S. Pister, *Comput. Meth. Appl. Mech. Eng.*, 1985, **51**, 177–208.
49 E. M. Arruda and M. C. Boyce, *J. Mech. Phys. Solids*, 1993, **41**, 389–412.
50 S. Govindjee and S. Reese, *J. Eng. Mater. Technol.*, 1997, **119**, 251–255.
51 B. D. Coleman and M. E. Gurtin, *J. Chem. Phys.*, 1967, **47**, 597–613.
52 T. J. R. Hughes, *The Finite Element Method: Linear Static and Dynamic Finite Element Analysis*, Prentice-Hall, 1987.
53 T. Belytschko, W. K. Liu and B. Moran, *Nonlinear Finite Elements for Continua and Structures*, John Wiley and Sons, 2002.
54 C. Miehe, *Comput. Meth. Appl. Mech. Eng.*, 1996, **134**, 223–240.
55 Tahoe, http://sourceforge.net/projects/tahoe/, 2011.
56 M. T. Shaw and W. J. MacKnight, *Introduction to Polymer Viscoelasticity*, John Wiley and Sons, 2005.
57 H. S. Park, Q. Wang, X. Zhao and P. A. Klein, *Computer Methods in Applied Mechanics and Engineering*, 2012, submitted.
58 A. G. Kusne and D. N. Lamberth, *IEEE Trans. Electron Devices*, 2010, **57**, 712–719.
59 T. D. Nguyen and S. Govindjee, *Int. J. Fract.*, 2006, **141**, 255–268.